Chapter 7

OPTICAL AND ELECTROCHEMICAL EFFECTS OF H_2 AND O_2 BUBBLES AT UPWARD-FACING SI PHOTOELECTRODES

Kempler, P. A., Ifkovits, Z.P., Yu. W., Carim, A.I., & Lewis, N.S. (2020). Optical and electrochemical effects of H_2 and O_2 bubbles at upward-facing Si photoelectrodes. *In preparation*

7.1 Introduction

Bubbles are generally regarded as deleterious to the performance of photoelectrochemical cells, and have been reported to act as concentrating “miniature lenses” that result in increased photocorrosion.[21, 126, 143] Bubbles are not optically absorbing, with a refractive index lower than their surrounding medium, and therefore primarily lead to the forward scattering of light.[144] In research laboratories, photoelectrochemical efficiency measurements are often performed on electrodes that are 0.1–1 cm^2 in area, which magnifies the scattering effects of mm-scale bubbles.[18] A few studies have directly quantified the optical effects of gas evolution.[145-147] H_2 bubbles led to > 20% reductions in the light-limited photocurrent density at small area upward-facing, platinized, planar p-Si photocathodes under simulated Air Mass (AM) 1.5 illumination.[145] Rising layers of O_2 bubbles with 40–50 μm radii have been reported to reflect 1–5 % of the incident illumination on a side-facing fluorine-doped tin oxide surface held at 1–8 mA cm^{-2} of current density.[147] However, the optical and electrochemical effects of surface-attached O_2 bubbles on upward-facing photoanodes have yet to be quantified, especially on large area electrodes that will be necessary in practical implementations of such devices.

Crystalline Si is well suited for studies of the nucleation and growth of gas bubbles during photoelectrochemical H_2(g) or O_2(g) evolution. Wet-chemical methods for preparing polished Si surfaces that have minimal densities of particles and organic contaminants have been well established by the microelectronics industry.[148] Si photocathodes are thermodynamically stable while evolving H_2 under cathodic conditions in 0.50 M H_2SO_4(aq).[149] When protected with conformal, thin films of TiO_2/Ni, Si photoanodes are stable for >100 h while evolving O_2 under anodic conditions in 1.0 M KOH(aq).[150] Si μW arrays have previously been shown in **Chapter 6** to influence the number density and radius of gas bubbles at downward-facing cathodes evolving H_2(g).[151]

Herein, ray-tracing simulations were combined with experimental measurements on cm-scale n-Si/TiO_2/Ni photoanodes and p-Si photocathodes to characterize the effects of H_2 and O_2 evolution on the optical and electrochemical performance of upward-facing photoelectrodes. Steady-state photoelectrochemical experiments at upward-facing planar and μW n-Si/TiO_2/Ni photoanodes have facilitated comparison of the influence of surface microstructure on the coverage and contact angle of gas-layers as well as resulting effects on the optical losses and ohmic resistance during device operation while evolving O_2(g). A dilute, redox-active tracer species was used to evaluate unassisted microconvection at upward-facing photoanode surfaces during O_2(g) evolution. Moreover, the nucleation rates and coverages of gas bubble layers were compared as a function of surface free energy at upward-facing hydrogen-evolving Si photocathodes. Ray-tracing simulations allowed the photocurrent density at upward-facing crystalline Si photoelectrodes to be predicted as a function of gas coverage, bubble radius, and contact-angle. Experiments at downward-facing p-Si photocathodes and downward-facing n-Si/TiO_2/Ni photoanodes allowed additional quantification of the coverage of surface-attached gas bubbles while concomitantly measuring their effect on the photocurrent behavior of such systems.

7.2 Experimental Methods

Detailed descriptions of materials, sample preparation methods, mass-transport measurements, and image analysis are provided in the Appendix.

Sample fabrication: N-type Si microwire arrays were fabricated via a deep reactive-ion etching process described previously, starting from a (100)-oriented P-doped Si wafers with a resistivity of 0.4 Ω-cm.[151] The wire diameter and pitch were defined by the photolithographically patterned etch mask. The holes in the masks had a nominal diameter of 6 μm; a center-to-center pitch of 14 μm or 28 μm; and the wires were etched to a height of 30 μm. All samples were cleaned via the "Standard Clean 1" and "Standard Clean 2" procedures developed by the Radio Corporation of America (RCA) to remove organics and metal contaminants, respectively (details on the cleaning procedures are provided in the Appendix, **A.1**).[148] 1000 cycles of of amorphous TiO_2 were deposited by atomic-layer deposition from a tetrakis(dimethylamido)titanium (TDMAT) precursor at a table temperature of 150 °C at a nominal deposition rate of 5.5 Å $cycle^{-1}$. Planar photoanodes were sputtered with 5 nm of Ni whereas Si microwire array photoanodes were sputtered with 10 nm of Ni, to ensure uniform coverage of the sidewalls of the microwires. Planar Si photocathodes were prepared from (100)-oriented B-doped Si wafers having a nominal resistivity of 10–20 Ω-cm. Hydroxyl-terminated p-Si surfaces were prepared via immersion in an RCA Standard Clean 1 bath for > 5 min, followed by rinsing in copious deionized water immediately prior to photoelectrochemical characterization. H-terminated p-Si surfaces were prepared via immersion in buffered oxide etchant (Transene) for > 10 s followed by rinsing in deionized water and drying in a stream of $N_2(g)$ immediately prior to photoelectrochemical characterization.

Upward-facing gas-evolution: Broad-spectrum illumination was provided by a 300 W ELH-type tungsten-halogen lamp with a dichroic rear reflector. The power supplied to the lamp was constant and the illumination intensity at the photoelectrode was controlled by the use of neutral density filters. The intensity of the lamp was measured by a NIST-traceable Si photodiode (Thorlabs, FDS100-Cal) mounted at the same position as the photoelectrodes but outside the electrolyte. Narrow-band illumination was provided by a light-emitting diode, LED, with an intensity-weighted average intensity at 630 nm (Thorlabs, M625L2). The emission intensity of the LED was modulated to set the light-limited photocurrent density, J_{ph}, at the photoelectrode. In alkaline electrolytes [1.0 M KOH(aq)], a Hg/HgO electrode in a Teflon casing was used as the reference electrode and a nickel wire behind a Fumasep FAAM-15 membrane (Fuel Cell Store) was used as a counter electrode. In acidic electrolytes [0.50 M $H_2SO_4(aq)$], a saturated calomel electrode behind a glass frit was used as the reference electrode and a Pt mesh behind a Nafion-117 membrane (Fuel Cell Store) was used as a counter electrode. The potential of the reference electrode in both cells was referenced to the reversible hydrogen electrode, RHE, as measured under 1 atm of $H_2(g)$ using a Pt wire coated with Pt black. The cell was open to the atmosphere and was filled with 0.100 L of electrolyte.

Downward-facing gas-evolution: The illumination sources, reference electrodes, counter electrodes, and separators were identical to those used in the upward-facing electrode experiments. Illumination provided by an LED was reflected into the cell using a Ag-coated mirror. The cell was open to the atmosphere and was filled with 0.050 L of electrolyte. Gas coverages were quantified by image processing in MATLAB (Appendix **A.7**).

Ray-tracing simulations: Simulations were performed using a ray-tracing program written in Python. The simulation was performed for a 2D slice of a 1 cm wide electrode covered by bubbles that were uniform in R_b and θ_b and distributed evenly across the surface. To approximate unpolarized light, the parent ray was initially weighted with equal field intensity in the in-plane and out-of-plane directions. Reflections obeyed the Fresnel equations and parent rays were resolved to 50 ray children, or until an individual ray contained 1% of the original ray power. An infinite absorber layer with an internal quantum yield of unity was assumed, so all rays entering the absorber produced electron-hole pairs that generated photocurrent.

7.3 Results

7.3.1 N-Si/TiO$_2$/Ni Photoanodes in 1.0 M KOH(aq)

The role of electrode microstructure on the behavior of gas bubbles was investigated over cm^2 areas using microfabricated electrodes having regular, micron-scale features. N-type Si microwires with uniform coatings of TiO_2 and Ni, n-Si/TiO_2/Ni, were prepared by atomic-layer deposition and RF-sputtering (**Figure 7.1A**). The TiO_2 provided a transparent, conducting protection layer against the corrosive electrolyte and the Ni served as a catalytic layer for the oxygen-evolution reaction.[150] The thickness of the TiO_2

and Ni at a planar substrate was 46 nm and 10 nm, respectively, as measured via ellipsometry. Planar n-Si/TiO_2/Ni photoanodes were prepared in the same fashion but were sputtered with 5 nm Ni. **Figure 7.1B-C** depict plan-view and cross-section scanning-electron micrographs (SEMs) of a microwire array with 6 µm diameter and 14 µm pitch, µW 6|14. SEMs of a µW 6|28 n-Si/TiO_2/Ni sample are provided as **Figure 7.1E-F.** The continuous etching process in the SF_6 and O_2 led to smooth sidewalls with a small amount of nanoscale roughness at the base of the array. The diameter at the tips and base of the wires was 6.1 ± 0.2 µm and 7.4 ± 0.2 µm, respectively, for the µW 6|14 array and was 6.1 ± 0.1 µm and 4.8 ± 0.2 µm, respectively for the µW 6|28 array.

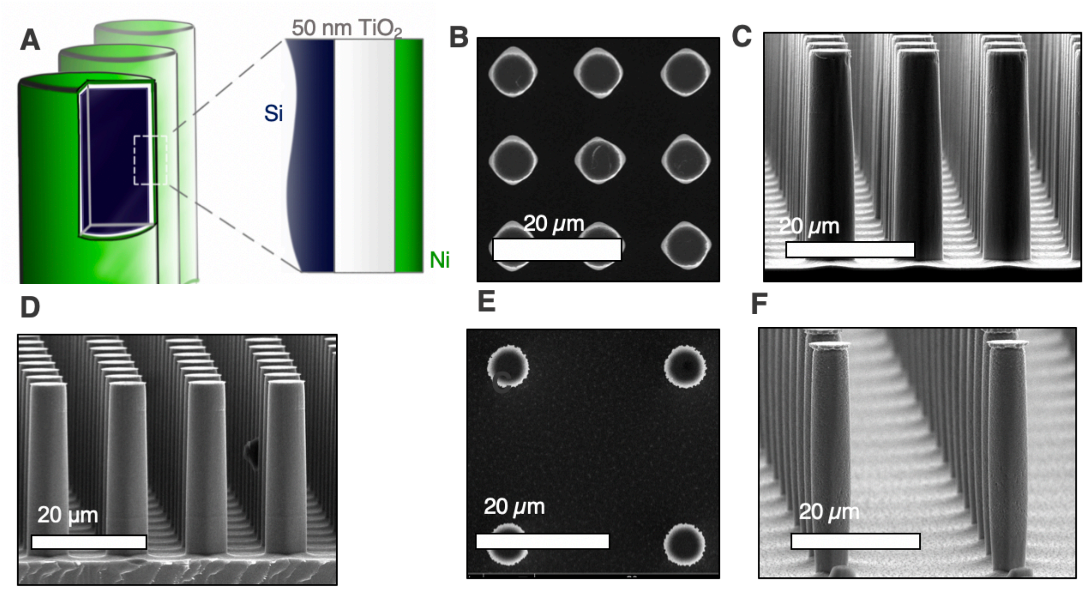

Figure 7.1: (**A**) Scheme of n-Si µW/TiO_2/Ni electrodes. Silicon (dark blue) was radially coated with TiO_2 (white) via ALD and Ni (green) via sputtering. (**B,E**) Plan-view scanning electron micrographs of (B) µW 6|14 and (E) µW 6|28 n-Si/TiO_2/Ni (**C,F**) Cross-section scanning electron micrographs of (C) µW 6|14 and (F) µW 6|28 n-Si/TiO_2/Ni. (**D**) Cross-section scanning electron micrograph of µW 6|14 p-Si.

The optical effects of O_2 bubbles on upward-facing electrodes were investigated for electrodes in 1.0 M KOH(aq). **Figure 7.2A** presents the current density vs potential, *J*-*E*, behavior of n-Si/TiO_2/Ni photoanodes under simulated 1-Sun conditions, as measured via linear-sweep voltammetry at a scan rate of 200 mV s^{-1}, before and after extended potentiostatic holds at 1.6 V vs RHE (**Figure 7.2B**). Data were not corrected for the substantial *iR* drop between the working and the reference electrode. Electrodes were poised at a potential at which *J* was light-limited, J_{ph}, producing conditions under which efficient charge separation produced by the potential drop across the space-charge region minimized effects due to changes in the exposed catalyst area, concentration overpotential, and/or electrolyte resistance. The thickness of the Ni layer on the planar n-Si/TiO_2/Ni was controlled so that microstructured and planar photoanodes yielded similar J_{ph} under nominally identical illumination conditions. Gas layers at oxygen-evolving n-Si/TiO_2/Ni photoanodes were characterized by large numbers of bubbles that released frequently at small radii. Under simulated 1-Sun illumination, J_{ph} was 20 mA cm^{-2} at either planar or µW 6|14 n-Si/TiO_2/Ni photoanodes, which produced streams of bubbles due to nucleation of bubbles predominantly at a small number of sites across the surface (**Figure 7.2C-D**). The number of nucleation sites increased as the illumination intensity increased, leading to a more uniform coverage of bubbles across the photoanode surface. The bubbles at the planar n-Si/TiO_2/Ni photoanode were larger in radius than the bubbles produced by µW 6|14 n-Si/TiO_2/Ni photoanodes.

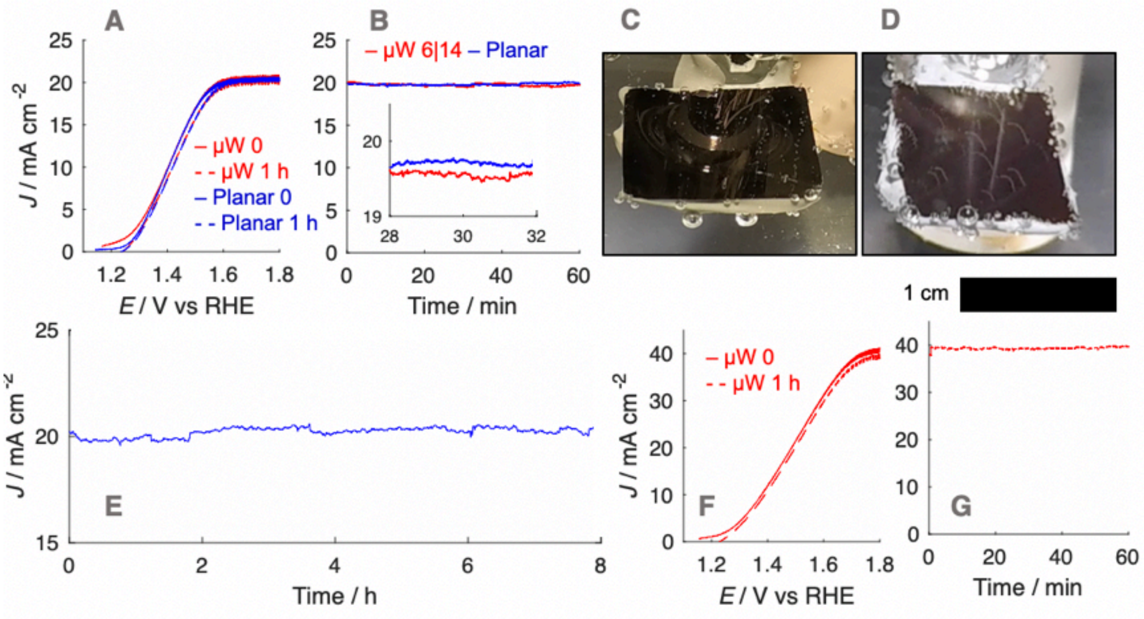

Figure 7.2: (**A**) *J-E* behavior for upward-facing planar (blue) and µW 6|14 (red) n-Si/TiO_2/Ni photoanodes in stagnant 1.0 M KOH(aq) recorded at 200 mV s^{-1} under illumination from an ELH type W-halogen lamp. Forward scans were recorded before (continuous) and reverse scans were recorded after (dashed) 1 h of continuous O_2 evolution at 1.6 V vs RHE. (**B**) J_{ph}-t behavior for photoanodes in (A), held at 1.6 V vs RHE. (**C,D**) Photographs of a (C) planar and (D) µW 6|14 n-Si/TiO_2/Ni electrode at J_{ph}=20 mA cm^{-2}. (**E**) Extended stability test of a planar n-Si/TiO_2/Ni electrode at 1.6 V vs RHE under illumination from an ELH-type W-halogen lamp in stagnant 1.0 M KOH(aq). (**F**) *J-E* behavior for an upward-facing µW 6|14 n-Si/TiO_2/Ni photoanode as in (A) following a doubling of the light intensity. (**G**) J_{ph}-t behavior of the photoanode in (F) at 1.8 V vs RHE.

The production of O_2 bubbles during gas evolution did not lead to a substantial change in J_{ph}, which remained stable and close to the measured maximum during voltammetry (**Figure 7.2A**). This J_{ph}-t behavior did not change during extended testing at 1.6 V vs RHE (**Figure 7.2E)**. Linear-sweep voltammograms after 1 h of continuous photoanodic operation showed that the *J-E* behavior was not substantially affected by the presence of a sparse gas bubble film. Illumination with 2-Suns of intensity yielded similarly stable J_{ph}-t behavior, consistent with the J-E behavior before and immediately after chronoamperometry (**Figure 7.2F-G**).

The effect of gas evolution on the Nernst diffusion layer was quantified for n-Si/TiO_2/Ni photoanodes in the presence of a dilute, redox-active tracer, $Fe(CN)_6^{4-}$, whose oxidation product, $Fe(CN)_6^{3-}$ strongly absorbs visible light (**Figure 7.3A**). Measurements were performed on both downward-facing and upward-facing electrodes. During photoanodic operation at 2.1 V vs RHE, J_{ph} was set by the illumination intensity from the LED. The average partial photocurrent passed towards $Fe(CN)_6^{4-}$ oxidation was calculated from the concentration of $Fe(CN)_6^{3-}$ measured in the cell after electrolysis. During the forward scan, two anodic peaks were observed, corresponding to surface oxidation of Ni and oxidation of $Fe(CN)_6^{4-}$. After electrolysis, these peaks were not present during the reverse scan (**Figure 7.3B**), indicating that the $Fe(CN)_6^{4-}$ concentration at the surface approached zero and that the electrochemically addressable nickel was fully oxidized. Measurements of the electrochemical behavior of $Fe(CN)_6^{4-}$ in 1.0 M KOH(aq) at a Ni wire and at Au wire are presented as **Figure A.7.1**. The Ni electrode was measured for comparison to the surface behavior of the n-Si/TiO_2/Ni photoanodes whereas the Au electrode measured the electrochemical behavior of $Fe(CN)_6^{4-}$ in the absence of surface redox waves.

Equation 7.1 relates the diffusion-limited current density for $Fe(CN)_6^{3-}$ production, $j_{\mathrm{Fe(III)}}$, to the bulk concentration of $Fe(CN)_6^{4-}$, $C_{\mathrm{Fe(II)}}$, and the mass-transport velocity, $m_{\mathrm{Fe(II)}}$, across the diffusion layer.

$$j_{\mathrm{Fe(III)}} = nFm_{\mathrm{Fe(II)}}\left[C^{*}_{\mathrm{Fe(II)}} - C^{0}_{\mathrm{Fe(II)}}\right] \qquad \mathbf{(7.1)}$$

where $C^{0}_{\mathrm{Fe(II)}}$, the concentration at the electrode surface, is assumed to be zero at sufficiently positive potentials. A detailed description of the mass-transport velocity measurements is provided in the Appendix (**A.7**). The mass-transport velocity at 1.3 V vs RHE, in the absence of oxygen evolution, was $4.17 \pm 0.06 \times 10^{-4}$ cm s^{-1}. The $< j_{\mathrm{Fe(III)}}>$ measured spectroscopically was within 3% of $<j_{\mathrm{Fe(III)}}>$ measured using chronoamperometry at 1.3 V vs RHE. Calculated values of $m_{\mathrm{Fe(II)}}$ were slightly larger for planar n-Si/TiO_2/Ni electrodes than for µW n-Si/TiO_2/Ni electrodes, and $m_{\mathrm{Fe(II)}}$ at upward-facing photoelectrodes was consistently larger than $m_{\mathrm{Fe(II)}}$ for downward-facing photoelectrodes (**Figures 7.3C**). The value of $m_{\mathrm{Fe(II)}}$ for downward-facing or upward-facing electrodes grew at an increasing rate when $J_{O2} > 20$ mA cm^{-2}, but for $J_{O2} < 20$ mA cm^{-2}, few bubbles were observed at the electrode surface and $m_{\mathrm{Fe(II)}}$ was only slightly larger than $m_{\mathrm{Fe(II)}}$ in a stagnant cell **(Figure 7.3C).**

Side-view, false colored photographs of illuminated gas streams emanating from upward-facing photoanodes (**Figure 7.3D-F**) revealed small streams of bubbles that were difficult to observe in top-down images. Fewer, larger bubbles were released on planar n-Si/TiO_2/Ni photoanodes (**Figure 7.3D**) than on µW 6|14 or µW 6|28 n-Si/TiO_2/Ni photoanodes **(Figure 7.3E,F)**. The vertical gas streams at µW 6|14 and µW 6|28 n-Si/TiO_2/Ni electrodes generated a horizontal flow of electrolyte at the electrode and at the electrolyte surface. Near the electrode surface, this flow was directed towards the center of the electrode, but at the electrolyte surface the flow was directed towards the edges of the electrode. $J_{\mathrm{ph}}/J_{\mathrm{ph}}^{\mathrm{bare}}$ was nearly constant with time, and for $J_{\mathrm{ph}} \leq 30$ mA cm^{-2} the optical losses did not exceed 2% of J_{ph} at a bare Si surface, despite substantial differences in the distribution of gas bubbles in the ~1 cm thick, illuminated layer of electrolyte.

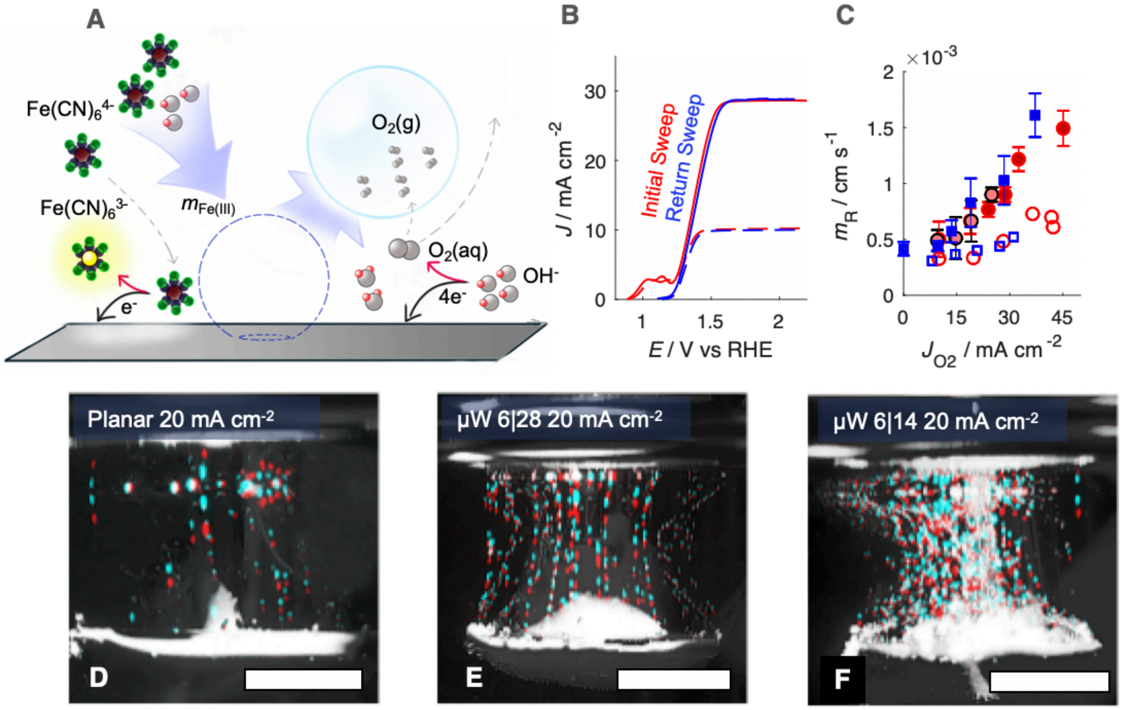

Figure 7.3: (**A**) Scheme of diffusion tracer experiments using $Fe(CN)_6^{4-}$ as a probe. OH^- and $Fe(CN)_6^{4-}$ are brought to the surface via diffusion and bubble-generated microconvection and contributed to Faradaic current. (**B**) *J-E* behavior of planar n-Si/TiO_2/Ni photoanode in 10 mM $Fe(CN)_6^{4-}$(aq), 1.0 M KOH(aq) before (red) and after (blue) a 5 min potential hold at 2.1 V vs RHE. (**C**) Mass-transport velocity as a function of anodic current density towards O_2 for planar, blue squares, μW 6|14 n-Si/TiO_2/Ni, dark-red circles, and μW 6|28 n-Si/TiO_2/Ni, light-red circles, photoanodes in 10 mM $Fe(CN)_6^{4-}$(aq), 1.0 M KOH(aq). Upward-facing measurements are shown by filled markers whereas downward-facing measurements are shown as open markers. Error bars on upward-facing measurements represent one standard deviation across three independent potential holds. (**D-F**) False-colored photographs of planar (D), μW 6|28 (E), and μW 6|14 (E) n-Si/TiO_2/Ni photoanodes during O_2 evolution in 10 mM $Fe(CN)_6^{4-}$(aq), 1.0 M KOH(aq) at J_{ph} = 20 mA cm^{-2}. Two frames separated by 50 ms were overlaid with changes highlighted in red and cyan, with red pixels representing the first frame and cyan pixels representing the second frame. All scale bars represent 5 mm.

Upward-facing planar or μW n-Si/TiO_2/Ni electrodes produced small coverages of gas bubbles that did not contribute to substantial increases in the ohmic resistance or concentration overpotential. (**Figure 7.2A,F).** Moreover, bubbles did not significantly reflect photons away from the semiconductor (**Figure 7.2B,E,G)**. The observation of gas bubble streams seen in this work has previously been reported at Pt microelectrodes in 1.2 M H_2SO_4(aq).[152] Gas evolution at upward-facing electrodes consistently led to increased $m_{\mathrm{Fe(II)}}$ relative to a stagnant electrolyte. Such behavior is consistent with previous measurements of the oxygen-evolving behavior of polished Ni foils.[153] The redox-active tracer used herein was present in concentrations that were 100-times more dilute than the concentration of OH^- in the cell, but yielded mass-transport-limited $j_{\mathrm{Fe(III)}}$ values only 10-times less than J_{ph} required for a 10% efficient solar fuels device.[115] This behavior suggests that the formation and departure of O_2 bubbles on upward-facing photoanodes generates sufficient convection to sustain device operation in unstirred electrolytes.

Mutually similar $m_{\mathrm{Fe(II)}}$ values were observed at upward-facing planar, μW 6|14, and μW 6|28 photoanodes (**Figure 7.3D-F**), despite the variation in the number density and radii of bubbles in the gas-layers. The dependence of mass-transport velocities only on the volumetric flow rate of gas, and not the size or distribution of gas bubbles. This is consistent with a fluid replacement model for bubble-generated microconvection.[153-154] Mass-transport velocities were lower at downward-facing electrodes relative to upward-facing electrodes (**Figure 7.3C**), suggesting that the departure rate of gas bubbles from the surface is a controlling variable on the microconvection process. A consequence of this microconvection model is that electrodes that produce isolated streams of gas bubbles (**Figure 7.3D,E**) will poorly mix the solution, with a spatially nonuniform distribution of reactants and products, potentially leading to undesirable pH gradients and efficiency losses. Increases in the density of microwires, from planar to µW 6|28 to µW 6|14, led to decreases in the radii of bubbles and an increased number of gas streams, which would be expected to lead to more uniform mass transport. Preexisting gas nuclei can also be added to the surface to ensure a more even distribution of passive microconvection.[155] To minimize concentration overpotentials and maximize the mass-transport velocity at the surface, solar fuels devices should maximize production of gas bubbles. In CO_2 reduction cells under nonconcentrated sunlight, the generation of highly reduced products such as C_2H_4 (12 e^- per mole) may not produce sufficient gas flow rates to eliminate the need for external convection at that electrode surface.

The low gas coverages and minimal decreases in J_{ph} in stagnant electrolytes observed for upward-facing Si photoanodes in 1.0 M KOH(aq) contrast with the previously reported behavior of side-facing or upward-facing planar Si photocathodes in H_2SO_4(aq), which exhibited higher coverages of larger bubbles than observed herein.[143, 145] The surface chemistry of planar photoelectrodes influences the gas coverage and consequently affects J_{ph}. The shape and departure diameter of a bubble is controlled by the adhesive forces at the solid/gas interface. The differences in R_b and θ_b between upward-facing photocathodes and photoanodes observed herein are not explained by differences in the surface free energy; both the hydrated $Ni(OH)_2$/NiOOH, which forms during photoanodic operation in 1.0 M KOH(aq), and clean noble metal surfaces, are expected to act as wettable, high-energy surfaces.[156-157] However, a monolayer of carbon contamination is sufficient to increase the hydrophobicity of a metal surface, and non-wetting behaviors have been reported at Au and Pt.[158] Rigorous cleaning may be required to observe similar nucleation rates at Si coated with a uniform layer of Pt. Hydroxyl terminated Si, Si/OH, is wettable and thus is expected to exhibit bubble contact angles approaching 180°.

7.3.2 Upward facing p-Si Photocathodes in 0.50 M H_2SO_4(aq)

To evaluate the gas-evolving behavior in the absence of the Ni catalyst and TiO_2 protection layers, upward-facing photocathodes prepared from planar p-Si that was either cleaned to a SiO_x/OH surface or to a Si–H surface were used as hydrogen-evolving photocathodes in 0.50 M H_2SO_4(aq). Photoanodes prepared from bare Si rapidly formed passivating SiO_x under anodic conditions. The J–E behaviors of upward-facing planar p-Si/OH and p-Si/H photocathodes in 0.50 M H_2SO_4(aq) were recorded using linear sweep voltammetry at 200 mV s^{-1} (**Figure 7.4A**). **Figure 7.4B** presents the time-dependent behavior of J_{ph} at upward-facing p-Si photocathodes maintained at E = –2.2 V vs RHE, which produced light-limited cathodic current densities. J_{ph} at upward-facing planar p-Si/OH electrodes was nearly identical to $J_{\mathrm{ph}}^{\mathrm{bare}}$, consistent with the absence of surface-attached gas bubbles (**Figure 7.4C**). In contrast, an upward-facing p-Si/H photocathode exhibited up to a 10% reduction to J_{ph} concurrent with a substantial coverage of gas bubbles on the electrode surface. The radius and coverage of gas bubbles at p-Si/H photocathodes decreased with time, and was accompanied by a gradual increase in J_{ph}.

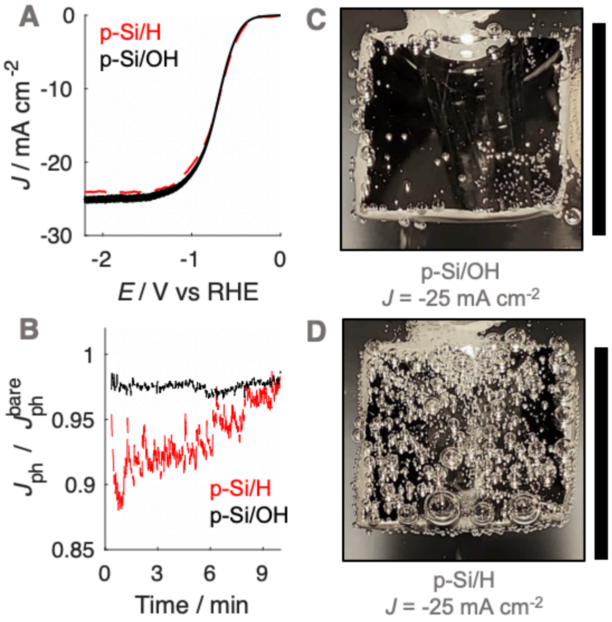

Figure 7.4: (**A**) *J-E* behavior for upward-facing p-Si photocathodes in stagnant 0.50 M H_2SO_4(aq) recorded at 200 mV-s under illumination from an ELH lamp. (**B**) *J-t* behavior for photoanodes in (A) at -2.2V vs RHE in 0.50 M H_2SO_4(aq). Top-down photographs of the (**C**) RCA-cleaned and (**D**) HF-cleaned planar p-Si photocathode shown in (B). Scale bars represent 1 cm.

A substantial reduction in the gas coverage was observed for hydroxyl-terminated upward-facing p-Si surfaces in 0.50 M H_2SO_4(aq) relative to hydride-terminated surfaces. This observation is consistent with heterogeneous nucleation rate models that include a dependence on the contact angle of the initial nuclei, because surfaces with $\theta_b \sim 180°$ are not catalytic for heterogeneous nucleation.[159] (100)-oriented Si surfaces terminated with Si-H bonds, following exposure to HF(aq), exhibit an advancing contact angle of > 70°,[160] and p-Si photocathodes dipped in HF exhibited gas coverages and J_{ph} losses in 0.50 M H_2SO_4(aq) that were comparable to those of Si coated with Ti/Pt.[145] For planar solar fuels devices that utilize a noble metal catalyst layer such Au or Pt, small R_b and θ_b values, approaching 180°, may be obtained after careful cleaning of such electrodes. Upward-facing polished Pt foils primarily produced bubbles < 100 μm in diameter after three days of continuous cathodic current flow in 1.0 M H_2SO_4(aq). Microstructuring or micropatterning can alleviate the deleterious effects of gas bubbles produced by non-optimal surface chemistry. Hence the results described herein are consistent with prior reports that the capillary forces within Si μW arrays, attributed to the more frequent release of small bubbles, lead to stable (photo)electrochemical performance in the absence of external convection.[151, 161] Patterned catalyst islands surrounded by a hydrophilic, passivating metal oxide layer could also result in increased wettability and decreased departure diameters for gas bubbles on upward-facing electrodes.

7.3.3 Ray-Tracing Simulations of Surface Attached Bubbles

Figure 7.5 summarizes the results of ray-tracing simulations of the optical characteristics of bubbles attached to crystalline-Si electrodes under 630 nm, unpolarized light. **Figure 7.5A** presents the theoretically predicted (*) light-limited photocurrent density, $J_{ph}*(r)$ as a function of the radial position, r, for a ray of infinitesimal thickness normalized to $J_{ph}*(r)$ predicted at a solid/liquid interface at normal incidence, J_{ph}^{bare}. A global minimum in $J_{ph}(r)$ should occur in a narrow ring at which total internal reflection at the liquid/gas interface directs rays away from the absorber. In contrast, a wider, local minimum in $J_{ph}(r)$ should occur for rays incident on the region above the solid/gas interface (**Figure 7.6**). Bubbles with a large contact angle, θ_b, (**Figure 7.6**) minimize the area of the solid/gas interface and should consequently reduce the magnitude of optical losses resulting from gas coverage. The simulations indicated a global maximum in $J_{ph}*(r)$ observed for bubbles with θ_b =160°, but not with θ_b =120°, due to a large number of reflections in the water layer adjacent to the solid/gas interface. Reductions in J_{ph} primarily result from reflections at the solid/gas interface, because reflected and refracted rays at the liquid/gas interface are predominately directed downwards towards the absorber.

The simulations also revealed that gas bubbles should produce a substantial redistribution of photogenerated carriers in the electrode (**Figure 7.5B**). Bubbles act as diverging lenses that should reduce the local J_{ph} but increase J_{ph} at locations removed from the bubble radius (**Figure 7.6A**). The highest regions of increased photocurrent were directly beyond the projected radius of a surface-attached bubble, with complementary effects for neighboring bubbles (**Figure 7.6B**). The sum total effect of gas films that contained multiple bubbles was simulated by line-scans over a 1 cm wide absorber, while varying the total coverage by bubbles having a uniform size and shape. Bubbles with larger values of θ_{b} minimized the area of the solid/gas interface for an equivalent projected surface coverage, producing values of $J_{\mathrm{ph}}*(r)$ close to $J_{\mathrm{ph}}^{\mathrm{bare}}$ (**Figure 7.5C**). Larger bubbles scattered light from a greater distance from the absorber surface and thus led to increased optical losses relative to an equivalent surface coverage of smaller bubbles (**Figure 7.5D**). However, gas coverages ≤ 0.5 produced a $< 10\%$ reduction in simulated J_{ph} values.

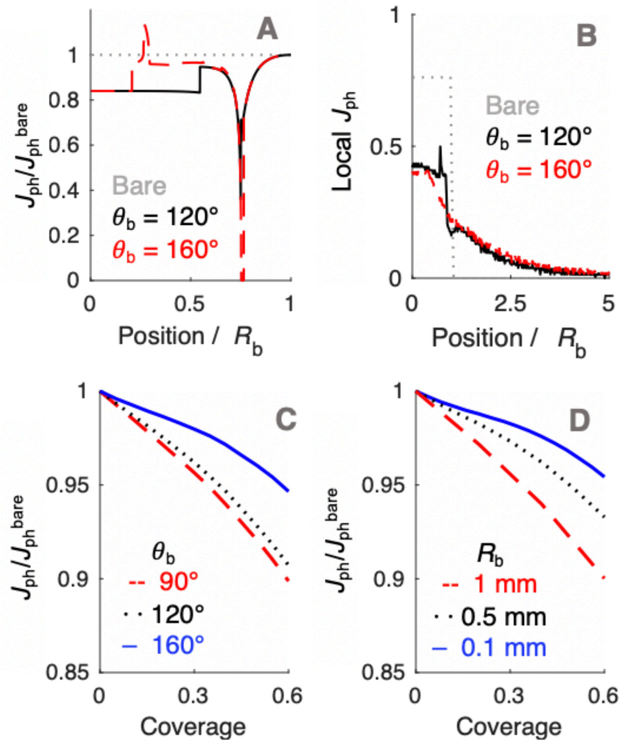

Figure 7.5: (**A**) Simulated $J_{ph}*(r)$ profile at a single bubble, for varied θ_b, normalized to the simulated J_{ph}^{bare} at the bare solid/liquid interface. (**B**) Distribution of $J_{ph}*(r)$ as measured via binned light absorption during ray-tracing simulations. The absorption is recorded as a function of position and the signal at individual bins was normalized to the total power incident on each bin in the absence of reflections or refractions. (**C**) Total $J_{ph}*$ at a 1 cm wide electrode as a function of gas coverage for bubbles with R_b = 250 μm and various values of θ_b. (**C**) Total $J_{ph}*$ at a 1 cm wide electrode as a function of gas coverage of bubbles with θ_b = 160° and various values of R_b.

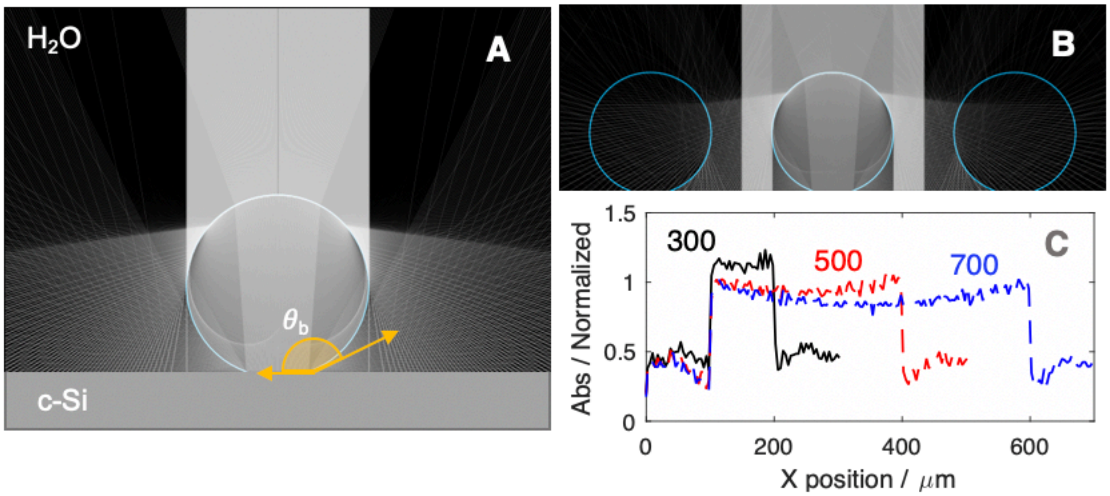

Figure 7.6: (**A**) Results of a ray-tracing simulation at a single surface-attached gas bubble, with θ_b = 160°, on crystalline silicon, illuminated by 630 nm unpolarized light, with liquid water as the surrounding medium. (**B**) Ray-tracing simulation for multiple, surface-attached gas bubbles with θ_b = 160°. (C) Absorption distribution at a surface containing bubbles with R_b = 100 µm and θ_b = 160° for varied center to center distances, recorded as a function of position. The absorption at individual positions, as bins, was normalized to the total power incident on each bin in the absence of reflections or refractions.

The close agreement between line scans of $J_{ph}*(r)$ simulated in this work and previously reported $J_{ph}(r)$ line scans measured experimentally using scanning-photocurrent microscopy demonstrates that ray-tracing simulations are an accurate method for simulating the optical properties of bubbles that have diameters substantially larger than a wavelength of light.[145] Although the shape of surface-attached bubbles can be expected to affect the spatial propagation of off-incident illumination (**Figure 7.5B**), J_{ph} should be close to J_{ph}^{bare} if R_b is small with respect to the electrode width (**Figure 7.5D**). Refracted rays are not scattered far from a bubble and can moreover produce an increase in collection efficiency relative to the absorption at a bare-Si/liquid interface (**Figure 7.5A**). **Equation**

7.2 gives the scattering distance, *s,* for a ray at position *r* undergoing total internal reflection as a function of the bubble radius, R_b, and θ_b:

$$s = R_b\left[\frac{2r\sqrt{1-r^2}}{2r^2-1}\left(\sqrt{1-r^2}-\cos\theta_b\right)\right] \tag{7.2}$$

where *r* has been normalized to represent the non-dimensional distance from the bubble center (**Figure 7.7A**). For a bubble with θ_b = 160°, the maximum scattered distance exceeds 10 R_b for the ring of light incident on $r \leq 0.76$ (**Figure 7.7B**). This region constitutes the global minimum observed in **Figure 7.5A**. The formation of gas bubbles with small radii on the surface serves two purposes in minimizing optical losses: (i) the maximum scattering distance is maintained within the width of the electrode and (ii) the projected area of the reflective ring on the solar flux plane is kept small. Anti-reflective layers and surface texturing could further minimize the optical losses at the gas/solid interface.[162]

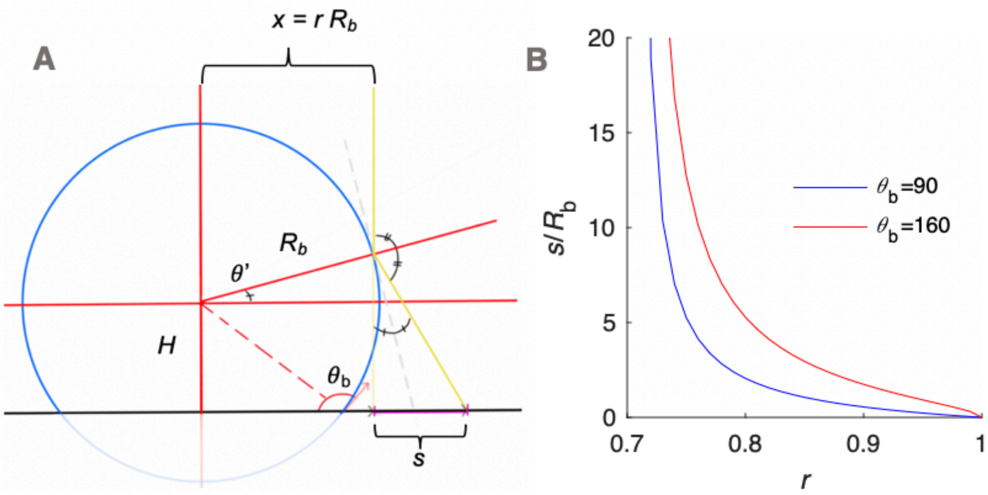

Figure 7.7: (**A**) Graphical representation of **Equation 7.2**. (**B**) Non-dimensionalized plot of the scattering distance (*s/R*) versus the ray position ($r = x/R$) for bubbles with θ_b = 90° and 160°.

7.2.4 Downward-Facing Photoelectrodes

To quantitatively evaluate the optical effects of static gas bubble films at the photoelectrode surface while controlling for the effect of departing gas bubbles in the electrolyte layer, the photoelectrochemical characteristics of downward-facing electrodes were investigated using 630 nm illumination (**Figure 7.8**). The gas coverage was measured from photographs and was compared against the instantaneous J_{ph} value determined directly before the gas coverage measurement (**Figure 7.8F-G**). Mutually equivalent rates of gas production were obtained by maintaining $J_{\mathrm{ph}}^{\mathrm{bare}}$ at -5 mA cm^{-2} for photocathodes (2 e- H_2 production) and at 10 mA cm^{-2} for photoanodes (4 e- O_2 production). Downward-facing planar and µW p-Si photocathodes exhibited larger bubble coverages than downward-facing n-Si/TiO_2/Ni photoanodes (**Figure 7.8A-B**). A maximum coverage of 0.57 was observed at downward-facing electrodes in 0.50 M H_2SO_4 with a minimum $J_{\mathrm{ph}}/J_{\mathrm{ph}}^{\mathrm{bare}}$ of 0.80 and 0.81 observed at p-Si and n$^+$p-Si/Ti/Pt electrodes, respectively (**Figure 7.8A**). The minimum $J_{\mathrm{ph}}/J_{\mathrm{ph}}^{\mathrm{bare}}$ value at downward-facing planar and µW 6|14 n-Si/TiO_2/Ni photoanodes was 0.96 and 0.94, respectively (**Figure 7.8B**).

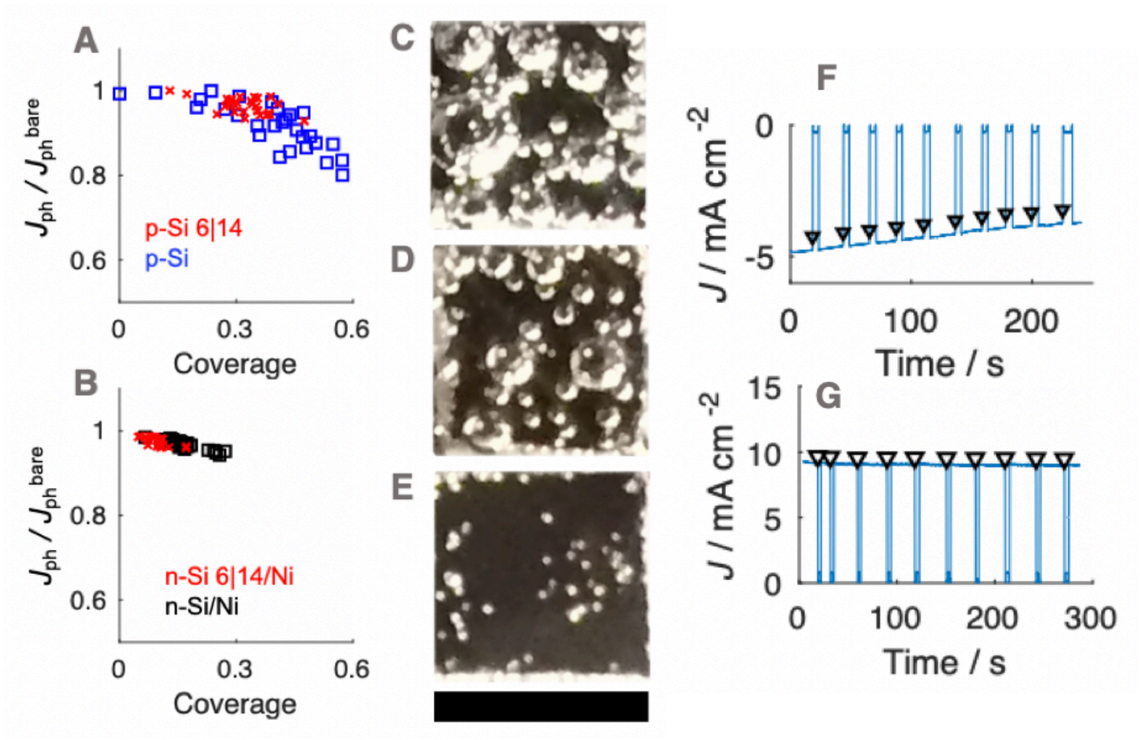

Figure 7.8: Coverage vs J_{ph}/J_{ph}^{bare} for downward-facing hydrogen-evolving photocathodes in 0.50 M H_2SO_4(aq) (A) and oxygen-evolving photoanodes in 1.0 M KOH(aq) (B). (C-E) Representative images of planar p-Si (C), µW 6|14 p-Si (D), and n-Si/Ni (E). Scale bars represents 5 mm. (**F**) *J-t* behavior of an inverted p-Si/H electrode under chopped illumination. The light source was turned off and an image was recorded under diffuse light at times marked with arrows. (**G**) *J-t* behavior of an inverted n-Si 6|14 electrode under chopped illumination.

The dependence of J_{ph}/J_{ph}^{bare} on the gas coverage (**Figure 7.8A-B**) was in agreement with simulated J_{ph}/J_{ph}^{bare} data vs coverage data for 2D line scans at coverages < 0.4 (**Figure 7.5C-D**). At the highest gas coverages, the experimentally measured J_{ph}/J_{ph}^{bare} values were lower than the J_{ph}/J_{ph}^{bare} values predicted by simulation, concurrent with the presence of the largest gas bubbles. The simulated gas coverages, however, assumed an even distribution of gas bubbles across the surface, whereas in practice gas bubbles tended to aggregate and were more often found near the edges of the electrode, which could increase the amount of light scattered away from the absorber. Differences in the shape of larger bubbles due to hydrostatic pressure could also influence the measured optical effects, but such effects are not expected to be relevant to the optical properties of bubbles at upward-facing electrodes.

The simulations described herein assumed that only bubbles that are large with respect to the wavelength of light contributed substantially to optical losses in photoelectrochemical cells, such that ray-optical treatment was sufficient to describe their optical properties. This assumption is justified by the $R \sim t^{1/2}$ dependence of bubble growth, such that bubbles spend a short time as small nuclei but spend a relatively long time close to the R_b at which the bubbles leave the surface.[163] The simulations in this work do not treat interference effects and will underestimate the effective scattering radius of small bubbles.[164] These effects could be important for solar fuels devices that generate a large number of small gas nuclei due to operation under concentrated sunlight.

The dominant optical effect of gas bubbles is the spatial redistribution of photogenerated carriers across the semiconductor surface. The deleterious effects of bubbles on the efficiency of small-scale photoelectrochemical solar fuels devices suitable for research-scale measurements cells are not present on larger-scale electrodes.[126] Solar fuels devices using a conductive emitter layer will redistribute carriers across the equipotential top surface such that bubbles will not affect the local J_{ph}.[165] Gas bubbles that are much smaller than the carrier-collection length of a semiconductor are unlikely to influence the spatial distribution of J_{ph} because photogenerated carriers will redistribute to minimize the overpotential at individual catalyst sites. Large gas bubbles on membraneembedded, electrically isolated microcells will have more substantial effects on the device efficiency if cells operating under less than 1-Sun illumination do not generate sufficient photovoltage to drive the full-cell reaction. Gas bubbles that adhere to micropatterned catalyst sites will direct light away from the catalyst, which could lead to beneficial increases in the total J_{ph}.

7.4 Conclusions

Simulations and experimental data confirm that forward-scattering optical effects of bubbles do not affect the total J_{ph} of a photoelectrochemical cell if R_b of the bubbles are kept small prior to departure from the surface. Careful preparation of metal and semiconductor surfaces could lead to θ_b approaching 180°, which will also minimize R_b. Solar fuels device designs should thus seek to maximize the wettability of the top-facing photoelectrode surface via control of the surface chemistry and/or microstructure, to obviate the need for surfactants such as Triton X-100 in the electrolyte.[21] Planar and microstructured n-Si/TiO_2/Ni photoanodes, ~1 cm^2 in area, exhibit gas coverages characterized by small R_b and large θ_b, and such devices exhibited minimal changes to J_{ph} during operation under 1 Sun equivalent illumination. Although the gas coverage increased substantially as the illumination intensity increased, J_{ph} remained stable with time. Gas evolution at upward-facing photoanodes in 1.0 M KOH(aq) led to increased mass-transport velocities compared to a stagnant electrolyte, and produces minimal concentration overpotentials adequate to facilitate efficient solar fuels device operation under non-concentrated sunlight, thereby eliminating the need for external convection